Applied Surface Science 599 (2022) 153971

Contents lists available at ScienceDirect

Applied Surface Science

journal homepage: www.elsevier.com/locate/apsusc

Full Length Article

Ionic liquid as morphology-directing agent of two-dimensional Bi_2WO_6: New insight into photocatalytic and antibacterial activity

Anna Pancielejko [a,b,*], Justyna Łuczak [a], Wojciech Lisowski [c], Grzegorz Trykowski [d], Danae Venieri [e], Adriana Zaleska-Medynska [b], Paweł Mazierski [b]

[a] Department of Process Engineering and Chemical Technology, Faculty of Chemistry, Gdańsk University of Technology, 11/12 G. Narutowicza St., 80-233 Gdansk, Poland
[b] Department of Environmental Technology, Faculty of Chemistry, University of Gdansk, 63 Wita Stwosza St., 80-308 Gdansk, Poland
[c] Institute of Physical Chemistry, Polish Academy of Science, 44/52 Kasprzaka St., 01-244 Warsaw, Poland
[d] Faculty of Chemistry, Nicolaus Copernicus University, 7 Gagarina St., 87-100 Torun, Poland
[e] School of Environmental Engineering, Technical University of Crete, 73100 Chania, Greece

ARTICLE INFO

Keywords:
Bi_2WO_6
2D structure
Nanosheets
Ionic liquid
Antibacterial properties

ABSTRACT

An efficient and durable utilization of light to drive photocatalytic reactions still requires the overcoming of barriers. Herein, two-dimensional (2D) ultrathin IL_Bi_2WO_6 (IL_BWO) photocatalysts were prepared for the first time *via* ionic liquid-assisted hydrothermal route by adjusting the amount of tetrabutylammonium chloride [TBA][Cl], synthesis temperature and duration. IL played the role of morphology-directing agent given by selecting the amount of IL, the control of nanosheet thickness was possible. The replacement of IL with KCl resulted in the growth of similar nanostructure, but with higher thickness, while, the absence of Cl^- caused the formation of clew-like microspheres. Two different model experiments, phenol degradation, and inactivation of *Escherichia coli* and *Staphylococcus aureus* bacteria were chosen to evaluate the photocatalytic activity. The improved photocatalytic performance was attributed to (i) the ultrathin structure, which let for shorter diffusion distance, (ii) the nitrogen presence in the photocatalyst structure, and (iii) the oxygen vacancies formation. The •OH and h^+ were the main species involved in the mechanism of photooxidation, and could be also responsible for the enhanced antimicrobial properties. The unique strategy of IL application establishes a new insight for a controllable preparation of 2D Bi_2WO_6 with improvement photocatalytic and antibacterial properties.

1. Introduction

Recently, the development of two-dimensional (2D) semiconductors has attracted a lot of attention in exploring the applications of heterogeneous photocatalysis, including water splitting [1], CO_2 reduction [2], bacterial disinfection [3], nitrogen fixation [4] and organic pollutants degradation [5]. Given by the outstanding size- and shape-dependent properties of 2D photocatalysts [6,7], such as (i) high developed specific surface area with abundant surface defects, (ii) shorter migration path to the photocatalysts' surface leading to minimalization of electron-hole recombination, (iii) improved conductivity, and (iv) excellent mechanical properties, numerous photocatalytic systems have been investigated [2,8–11].

Meanwhile, layered bismuth-based photocatalysts have become promising 2D materials due to their suitable band gaps (usually below 3.0 eV), high efficient in photocatalytic reaction under visible light irradiation, and negligible toxicity [11,12]. As one of the simplest Aurivillius oxide, bismuth tungstate (Bi_2WO_6) with a layer structure of $[BiO]^+$-$(WO_4)^{2-}$-$[BiO]^+$, has been considered as a good candidate [13]. However, pristine Bi_2WO_6 usually possesses low photocatalytic efficiency and selectivity attributed to the rapid recombination of photogenerated charge carriers between the Bi6s and O2p orbitals and the W5d orbital. An effective charge separation could play a significant role in the electron transport from the inside layer to the photocatalyst surface. Thereby, efforts have been made to manipulate the electronic states and enhance the photocatalytic performance. Those modifications resulted in altering the band gap positions of the favoured redox potential, improving the harvest of light, and strengthening the interaction

* Corresponding author at: Department of Process Engineering and Chemical Technology, Faculty of Chemistry, Gdańsk University of Technology, 11/12 G, Narutowicza St., 80-233 Gdansk, Poland.
E-mail address: anna.pancielejko@pg.edu.pl (A. Pancielejko).

https://doi.org/10.1016/j.apsusc.2022.153971
Received 25 January 2022; Received in revised form 23 May 2022; Accepted 12 June 2022
Available online 18 June 2022

between 2D photocatalysts and adsorbed compounds [13–16]. Considering the literature data, it can be concluded that a key in design of efficient 2D Bi_2WO_6 photocatalytic systems could be achieved by size and architectural control as well as by surface/structure modifications. Nonetheless, the effect of the synthesis conditions on the growth and morphology of 2D Bi_2WO_6 has been rarely described.

Currently, a number of reports focus on the synthesis of 2D Bi_2WO_6 without template [17] or with surfactant assistance [13,18]. Meanwhile, one of the new approaches in controlled fabrication of 2D photocatalysts is the application of ionic liquids (ILs). Their unique physical and chemical properties (*e.g.,* negligible vapour pressure, low melting point, high thermal, and chemical stability) makes ILs an interesting media in micro- and nanostructure synthesis [19,20]. Recent findings suggest that ILs could facilitate the growth of photocatalysts composed of isolated few- or single-layer nanosheets [21,22]. Moreover, it is suggested that the presence of IL in the reaction environmental could influence on the enhancement photoactivity of 2D photocatalysts due to the doping of nonmetal elements originated from IL organic cations, similar like in three-dimensional (3D) nanomaterials. Until now, only bismuth oxyhalides [22,23], bismuth molybdate [24], bismuth selenide [25], and bismuth-based composites [26,27] were prepared in the presence of ILs. However, there is no report about the IL-assisted synthesis of 2D layered Bi_2WO_6. Although, the photoactivity of abovementioned photocatalysts against several organic contaminants has been report, there is lack of information regarding their antibacterial properties. Meanwhile, it is speculated that in view of the tuneable nature and antimicrobial qualities of ILs-assisted photocatalyst, the presence of IL residues could affect for an enhanced inactivation Gram-negative and Gram-positive bacterium.

Considering the above aspects, for the first time, a fine characterization of 2D IL_Bi_2WO_6 (IL_BWO) was performed by adjusting the amount of tetrabutylammonium chloride [TBA][Cl], reaction temperature, and duration. The beneficial properties of IL-regulated BWO photocatalysts were explored due to their morphology, structure, and surface composition toward the photocatalytic degradation of organic contaminant and antibacterial purposes. IL played the role of morphology-directing agent given by selecting the amount of IL, the control of nanosheet thickness was possible. In addition, the ability to remove organic pollutant was evaluated as a function of monochromatic irradiation to determine the exact range of the photoactivity. Based on the obtained results, the possible mechanism of growth and photocatalytic reaction over ultrathin IL_BWO nanosheets was proposed.

2. Experimental section

2.1. Materials

All reagents were of analytical grade and used without any additional purification. Bismuth(III) pentahydrate ($Bi(NO_3)_3 \cdot 5H_2O$, ≥98.0% purity, Sigma Aldrich, Germany), sodium tungstate dihydrate ($Na_2WO_2 \cdot 2H_2O$, ≥99% purity, Sigma Aldrich, Germany), potassium chloride (POCH S.A., Poland), tetrabutylammonium chloride [TBA][Cl] (Iolitec, Germany, purveyed with ≥97% of purity), nitric acid (POCH S. A., Poland) and deionized water (DI, with conductivity of 0.05 μS) have been applied.

2.2. Preparation of the BWO photocatalysts

The synthesis was carried out as following: (1) $Bi(NO_3)_3 \cdot 5H_2O$ (2 mmol) was dissolved in 0.1 M HNO_3 solution (80 mL); (2) the mixture was placed under sonication for 10 min; (3) $Na_2WO_4 \cdot 2H_2O$ (1 mmol) and [TBA][Cl] were added followed by vigorous magnetic stirring for 30 min (the molar ratio of IL: Bi precursor was variable and range from 1:10, 1:14, 1:20, 1:25 to 1:30 while amount of $Bi(NO_3)_3 \cdot 5H_2O$ and $Na_2WO_4 \cdot 2H_2O$ were constant). Afterwards, the mixed solution was poured into a Teflon-lined stainless-steel autoclave and kept at 120 °C for 24 h. Additionally, the processes were performed at the temperatures of 100, 140, and 160 °C for 24 h and at 120 °C for 3, 6, and 12 h (for 1:20 M ratio of IL: $Bi(NO_3)_3 \cdot 5H_2O$). After cooling to room temperature, the as-prepared powders were washed several times with deionized water and dried overnight at 60 °C. For comparison, BWO with KCl addition instead of IL (in a molar ratio of KCl: Bi precursor 1:20), while keeping other parameters unchanged, was synthesised. Pristine BWO was prepared without [TBA][Cl] or KCl assistance.

2.3. Surface properties characterization

Electron microscopy measurements were made using two SEM microscopes (Quanta 3D FEG, FEI Company, Brno, Czech Republic, which imaged in STEM mode and SEM, JSM-7610F, JEOL, LTD, Tokyo, Japan, working in HRSEM mode) and TEM microscope (Tecnai G2 F20X-Twin, FEI Company, Brno, Czech Republic). TEM imaging was taken in bright field (BF) and diffraction images were recorded in selected-area electron diffraction (SAED) mode. The samples for SEM measurements were placed on the carbon tape attached to the SEM specimen stub, and the samples were to be measured TEM and STEM were prepared by proceeding with sonication for 5 s (a few milligrams of sample in 99.8% anhydrous ethanol using ultrasound), then applying a drop (5 μL) on a carbon coated copper grids with holes (Lacey type Cu 400 mesh, Plano) and evaporating the solvent at room temperature. Powder X-Ray diffraction (XRD) analysis was carried out with the Rigaku MiniFlex 600 X-ray diffractometer with Cu Kα radiation (λ = 1.5405 Å) in the range of 10-80° (step 1°/min) to determine the crystalline structure. The optical system adopts focusing geometry used in powder XRD generally (equipped with a scintillation counter) and irradiates the sample with divergent X-rays limited by a divergent slit (a Bragg-Brentano geometry). Standard resolution receiving soller slit (5.0°) was used. The investigation was performed with the HighScorePlus software package (PANalytical, 2006) and program REFINE (Version 3.0, 1998). The BET surface area and pore sizes were evaluated by using a Micromeritics Gemini V200 Shimadzu analyzer with the VacPrep 061 Degasser supply. All samples were degassed at 200 °C for 2 h prior to nitrogen adsorption measurements. The BET surface areas were evaluated by the multipoint BET method using adsorption data for relative pressure (p/p_0) range of 0.05–0.3. Raman spectra were collected by Thermo Scientific DXR Smart Raman spectrometer with a 532 nm laser as the excitation source at ambient conditions. The Zeta potential was investigated with Zetasizer Nano ZS (Malvern, USA) in distilled water (pH 7). X-ray photoelectron spectroscopic (XPS) measurements were performed for examining the chemical state of the elements at the surface of selected samples. The XPS analysis were carried out on a PHI 5000 Versa Probe (ULVAC-PHI, Chigasaki Japan) scanning spectrometer with monochromatic Al Kα irradiation (hν = 1486.6 eV) from an X-ray source operating at 100 μm spot size, 25 W and 15 kV. The prepared powder materials were analyzed using a modified PREVAC sample holder [28] (standard sample holder equipped with a plate adaptor of powder holding containing a cylinder pocket, 3 mm diameter, 1 mm depth). The high-resolution (HR) XPS spectra were recorded with the hemispherical analyser at the pass energy of 23.5 eV, the energy step of 0.1 eV and the photoelectron angle of 45° with respect to the surface plane. Charge compensation was achieved using a PHI's patented dual beam charge neutralization system [P. E. Larson and M. A. Kelly, U.S. patent 5,990,476A (November 23, 1999), JP patent P3616714B2 (February 2, 2005), and EP patent 0848247B1 (July 3, 2002)]. Casa XPS software (v.2.3.19, Casa Software Ltd, Wilmslow, United Kingdom) was used to evaluate the XPS data. Shirley background subtraction and peak fitting with Gaussian–Lorentzian-shaped profiles was performed. Binding energy scale was referenced to the C1s peak with BE = 284.8 eV. For quantification the PHI Multipak sensitivity factors and determined transmission function of the spectrometer were used. UV–Vis diffuse reflectance spectroscopy (DRS UV–Vis) was used to record the absorption spectra (Evolution 220, Thermo Scientific) in the wavelength range

of 200–800 nm, equipped with an integrating sphere. The baseline was made for the standard barium sulphate, and the scanning speed was 200 nm • min^{-1} at room temperature. Photoluminescence spectroscopy was determined by a LS-50B photoluminescence spectrometer (Perkin Elmer Ltd.) equipped with a xenon discharge lamp as the excitation source and an R928 photomultiplier as the detector. The spectra were determined in the range of 300–700 nm at an excitation wavelength of 300 nm directed on the sample surface at an angle of 90°.

2.4. Photocatalytic evaluation

The photocatalytic activity tests were carried out in a cylinder reactor with a quartz window filled with the mixture of 0.125 g of the photocatalyst in 25 mL of aqueous phenol solution (20 mg/L). The irradiation was performed by a 1000 W Xenon lamp (Oriel 66021) emitting UV–Vis light ($\lambda > 350$ nm). To establish the absorption–desorption equilibrium, the reactor was kept without light for 30 min. Subsequently, the mixture was irradiated for 60 min with continuous magnetic stirring (450 rpm) and air aeration (5 dm^3/h) with UV–Vis light. The temperature in the reactor during the process was thermostatically controlled by a water bath and maintain at 10 ± 0.5 °C. Reference phenol samples (0.5 mL) were taken every 20 min during the process. To remove the fine particles from the sample, the mixture was filtered through a 0.2 μm syringe filter. The efficiency of the phenol degradation was analysed with high performance liquid chromatography (HPLC, Shimadzu) equipped with a Kinetex C18 column (150 × 3 mm, particle size 2.6 μm, pore diameter 100 Å) and SPD-M20A diode array detector operated at 225 nm. The mobile phase was composed of acetonitrile and trifluoroacetic acid (10/90, v: v) with a constant flow rate of 0.55 mL/min. The blind test in the absence of photocatalysts resulted in negligible low phenol degradation. Consequently, the phenol decomposition intermediate's concentration was investigated as above-mentioned and detected at 254 nm. The photostability measurements were carried out in four consequently cycles. After each process, the suspension was centrifuged. Subsequently, the recovered photocatalyst was put in the reactor and filled with the fresh portion of phenol solution. Besides, the methodology was similar to that of that photocatalytic activity measurements.

The active species trapping experiments employing benzoquinone, ammonium oxalate, *tert*-butanol, and silver nitrate in the aqueous phenol solution (20 mg/L, 1:1 v/v) were performed. Besides, the procedure was similar to that described above for the photoactivity measurements.

Action spectra (AS) measurements were carried out under monochromatic irradiation by a diffraction grating illuminator (Jasco, RM-FD). The photocatalyst (0.04 g) was put in a quartz reactor filled with aqueous phenol solution (20 mg/L, 10 mL). The photoreactor was kept in the dark for 30 min to achieve adsorption–desorption equilibrium and then irradiated by 300 W Xenon lamp (Hamamatsu C2578-02) with tuneable monochromatic wavelengths (in the range of 380–560 nm) for 210 min with continuous magnetic stirring and aeration (20 dm^3/h) under ambient temperature. An optical power meter (HIOKI 3664) was used to measure the intensity of irradiation at each wavelength. During the experiments, 0.5 mL of the suspension was taken every 30 min and filtered through a 0.2 μm syringe filter. The concentration of benzoquinone was monitored by HPLC analysis (the same conditions to those described above). The apparent quantum efficiency (AQE) was estimated as the ratio of the reacted electrons to the number of absorbed photons in accordance with the reaction stoichiometry.

2.5. Antibacterial activity

The bacteria inactivation experiments were performed in the presence of the obtained photocatalysts (250 mg/mL) for two kinds of bacteria strains by reference type of *Escherichia coli* (*E. coli,* German Collection of Microorganisms and Cell Cultures, DSMZ) and wild strains of *Staphylococcus aureus* (*S. aureus,* identified by bioMérieux's API@S-taph*)* in an open, cylindrical glass containing sterile 0.8% NaCl aqueous solution (198 mL) and inoculated bacteria cells (2 mL, 10^3 Colony Forming Units (CFU/mL). The reaction mixture was maintained for 20 min in the dark to establish the absorption–desorption equilibrium, followed by the irradiation with UVA lamp (Sylvania, Blacklight 368, F 15 WOT8IBL368, Germany) for 180 min with an intensity of 11.5 mW/cm^2 (Oriel 91150 V) under continuous magnetic stirring conditions (300 rpm) at 24 °C. The reaction mixture samples were collected after each 60 min of the process (1 mL) and streaked onto the nutrient agar (200 μL). The bacteria colonies were counted after incubation for 20–24 h at the temperature of 37 °C. The control experiments in darkness in the presence of each photocatalysts, as well as the blank test (in the absence of photocatalysts) in darkness and under UVA irradiation were also performed.

3. Results

IL_Bi_2WO_6 (IL_BWO) samples were successfully synthesized through a simple hydrothermal process. In this work, particular attention was given to the effect of [TBA][Cl] amount on the morphology, photocatalytic and antibacterial properties of the obtained products under variable synthesis temperatures and duration. The sample code, molar ratios of the reagents, synthesis conditions, surface parameters, band gaps, and photoactivity under UV–Vis irradiation of the IL_BWO samples are listed in Table 1.

3.1. Characterization of the photocatalysts

The morphology of the IL_BWO samples was investigated by SEM, STEM and TEM observations (Figs. 1 and 2). As shown in Fig. 1a, pristine BWO photocatalyst consisted of clew-like microstructures with diameter of 3.39 ± 0.49 μm. Higher magnification images showed that each clew was constructed of irregular spaced threads with thickness of 36 ± 16 nm. The analysis of samples synthesised in the presence of IL revealed formation of the dish composed of criss-crossed nanosheets. Increase of the IL content in the reaction environment resulted in the reduction of the diameter from 2.17 ± 0.43 μm to 1.38 ± 0.31 μm for IL_BWO5 and IL_BWO1, respectively (Fig. 1c-e). In addition, it was found that by selecting the amount of IL, the control of nanosheet thickness was possible. The highest nanosheet thickness was observed when the highest amount of IL was used for the reaction (14 ± 4 nm for IL_BWO1). Noteworthily, even the smallest addition of IL resulted in the growth of criss-crossed nanosheets with the thickness of 10 ± 3 nm (IL_BWO5). The optimal amount of IL causing growth of the ultrathin nanosheets (8 ± 2 nm for IL_BWO3) was found for 1:20 M ratio. In order to assess the role of IL in shaping morphology, the analysis of the sample obtained in the presence of KCl (KCl_BWO) was investigated (Fig. 1b). The addition of inorganic chloride salt during the reaction led to the growth of similar to the IL_BWO dish-like structure with the following morphological parameters: the diameter of 2.40 ± 0.47 μm and nanosheets thickness of 13 ± 6 nm. Worth to highlighted, that the addition of both [TBA][Cl] and KCl resulted in the reduction of diameter and nanosheets thickness in comparison with pristine BWO (Fig. 2). It suggests that the layered structure could be achieved by controlling the concentration of those both additives interchangeably. Although, it can be seen that the application of IL reduced not only the diameter and nanosheets thickness, but also increased the rough surface, and thus could provide larger amounts of mesopores and induce larger surface area than that of KCl_BWO (Fig. 2). Thereby, it was concluded that the source of Cl^- ions played significant role in the nanosheets forming since the presence of the surface repulsion forces and steric hindrance from the IL cation prevented the layers from stacking (see insets in Fig. 1b and d). Similar feature was observed previously where the layered arrangement of Bi_2MoO_6 and Bi_2WO_6 were controlled by CTAB amount [13,29].

In this study, particular attention was given to the effect of this IL

Table 1
Sample code, molar ratio of reagents (IL/KCl: Bi precursor), synthesis conditions, surface properties, band gap energies, and phenol degradation under UV–Vis irradiation of IL_BWO photocatalysts.

No.	Sample code	Type of structure	Molar ratio of IL: Bi precursor	Molar ratio of KCl: Bi precursor	Time of the synthesis (h)	Temperature of the synthesis (°C)	Specific surface area ($m^2.g^{-1}$)	Pore volume ($cm^3.g^{-1}$)	Band gap (eV)	Phenol degradation efficiency under 60 min of UV–Vis irradiation (%)
1	BWO	clew like	–	–	24	120	39.51	0.0195	2.93	38
2	KCl_BWO	"dish" with	–	1:20			49.26	0.0240	3.04	22
3	IL_BWO1	criss-crossed	1:10	–			55.57	0.0270	3.08	41
4	IL_BWO2	nanosheets	1:14				52.81	0.0257	3.03	45
5	IL_BWO3		1:20				47.60	0.0232	3.03	86
6	IL_BWO4		1:25				45.45	0.0221	3.01	36
7	IL_BWO5		1:30				44.86	0.0220	3.04	26
8	IL_BWO6		1:20			100	29.67	0.0292	3.15	39
9	IL_BWO7					140	35.87	0.0173	3.04	55
10	IL_BWO8					160	30.26	0.0145	3.03	14
11	IL_BWO9				3	120	40.16	0.0200	3.25	18
12	IL_BWO10				6		40.93	0.0202	3.14	23
13	IL_BWO11				12		57.43	0.0279	3.06	28

*The IL_BWO3 sample, synthesised in a molar ratio of IL: Bi precursor of 1:20 for 24 h at 120 °C, was prepared in each series to compare the influence of the synthesis conditions.

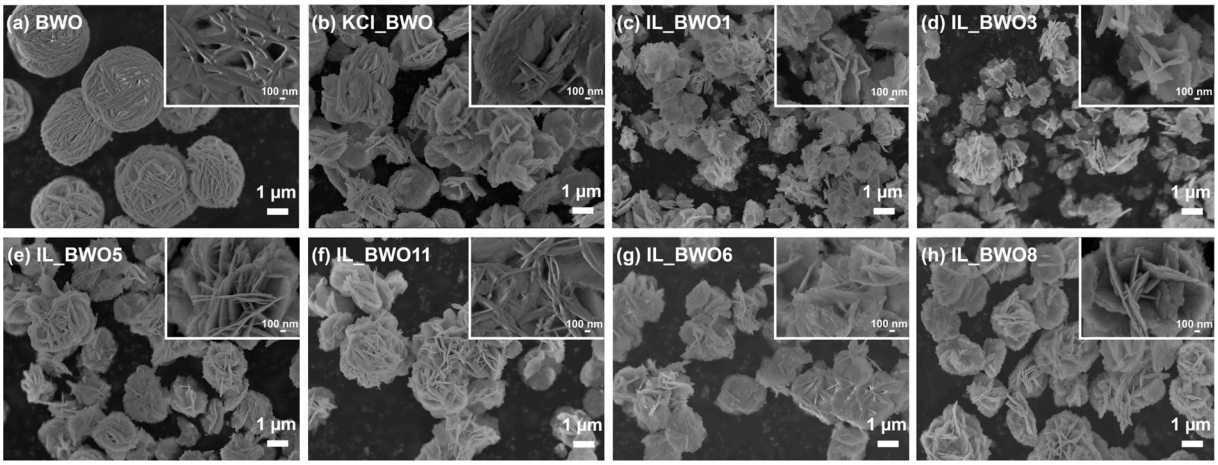

Fig. 1. SEM images of the selected samples: (a) BWO, (b) KCl_BWO, (c) IL_BWO1, (d) IL_BWO3, (e) IL_BWO5, (f) IL_BWO11, (g) IL_BWO6, and (h) IL_BWO8. The insets in the upper right corner are the corresponding SEM images with high magnification.

amount which led to the growth of the BWO nanosheets with the lowest thickness (molar ratio of IL: Bi precursor 1:20) and was used to investigate the influence of other synthesis conditions (reaction temperature and duration). Regarding the literature, it is expected that the ultrathin nanosheet structure could result in the enhanced photocatalytic performance [13,18,30]. The SEM images of the selected samples prepared in various conditions are shown in Fig. 1f-h. It was found that the particles size and shape of the IL_BWO photocatalysts were quite different depended on the synthesis conditions. The IL_BWO11 sample, hydrothermal treated for 12 h, was composed of the nanosheets thickness of a dozen nanometres arranged in hierarchical flower-like structure (Fig. 1f). When the reaction time was prolongated to 24 h, the nanoparticles started to agglomerate into smaller nanoparticles consisted of the ultrathin nanosheets (Fig. 1d). With lowering the synthesis temperature to 100 °C, the obtained IL_BWO6 sample also exhibited dish-like architecture with criss-crossed nanosheets but these nanosheets were uncomplete formed, broken and folded (Fig. 1g). At the highest applied temperature, 160 °C, the obtained IL_BWO8 sample exhibited the dish like structure too, however, a close observation of the higher magnification SEM image revealed that each layer was made up by many nanoplates packed in the criss-crossed structure (inset in Fig. 1h).

By observing the morphological changes, the possible mechanism of the IL_BWO photocatalysts formation was proposed. After ultrasonically treatment, $Bi(NO_3)_3{\cdot}5H_2O$ was completely dissolved, thus Bi^{3+} ions were present in the acidic reaction mixture. When $Na_2WO_4{\cdot}2H_2O$ was added regular clew-like microspheres were formed. After introducing to the reaction environment IL, [TBA][Cl], an unstable Bi^{3+}-IL complex would occurred firstly, which was gradually decomposed when the reaction goes on. Slowly realised Bi^{3+} ions reacted with WO_4^{2-} ions present in the mixture, leading to the formation of dish-like BWO structures constructed of criss-crossed nanosheets. It can be inferred that during the dissolution–recrystallization process, the presence of IL residues in the reaction mixture might result in their absorption on the BWO surface and provide formation of active sites for nanocrystalline growth. Thereby, the number of active sites on the BWO surface might be variable depending on the IL amount used during the synthesis, and thus affected not only morphological but also photocatalytic properties, and will be discussed later.

The crystalline phase of the synthesized photocatalysts was identified by X-ray diffraction analysis (Fig. 3a and S1). All patterns were indexed to the crystal structure as orthorhombic Bi_2WO_6 crystal phase (R060860 Bi_2WO_6, Russellite). No existence of other peaks implied high purity of the as-prepared samples. The photocatalysts prepared with Cl^- ions, originated from IL or KCl, showed weaker diffraction peak intensity than pristine BWO, suggesting the smaller size and thickness of those sample, in agreement with the morphology results discussed above (Fig. 2). Moreover, the XRD pattern of the photocatalyst prepared in the presence of KCl was similar to that of prepared with [TBA][Cl]

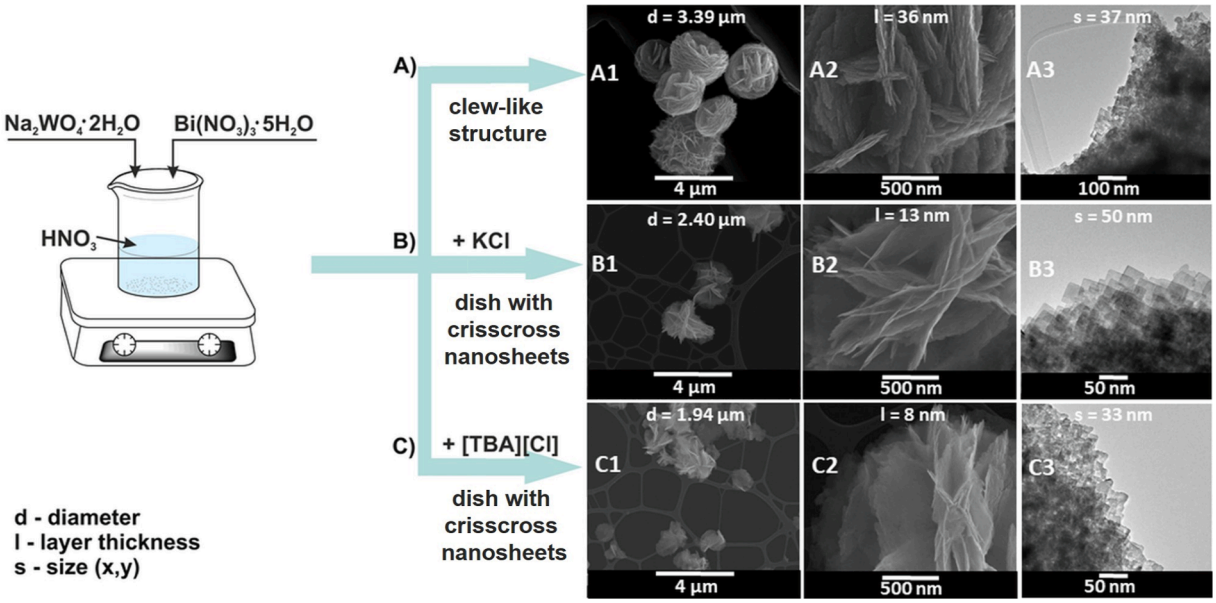

Fig. 2. Schematic diagram illustrating the morphological changes and their dimensions (diameter, thickness and size) in A) pristine BWO, B) KCl_BWO, and C) IL_BWO3 (A1, A2, B1, B2, C1, C2 - STEM images; A3, B3, and C3 – TEM images with different magnification).

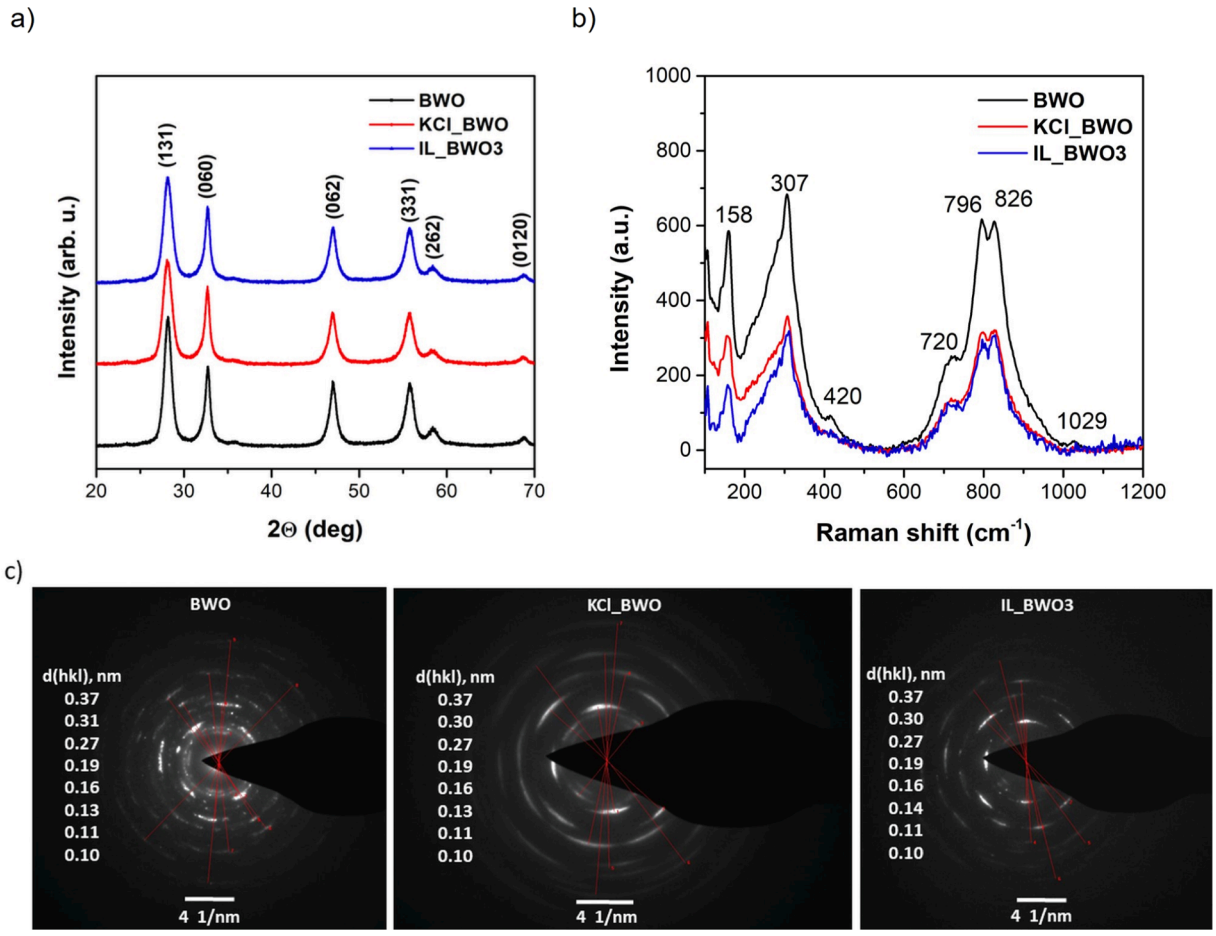

Fig. 3. (a) XRD patterns, (b) Raman peaks, and (c) SAED images of the selected photocatalysts.

assistance (IL_BWO3) implying a very similar crystal phase. Taking into account the influence of the synthesis conditions, it was found that such small changes in the amount of applied IL negligible affected on the diffraction peak intensities, and thus the crystal structure (Fig. S1a). A linear increase in the relative intensity of the diffraction spectrum was observed with increase of the reaction temperature in the range of 100–160 °C. As revealed, the reaction temperature of 100 °C was too low to form crystal phase (Fig. S1b). Formation of BWO was also difficult

when the reaction duration was shorter than 12 h (Fig. S1c). The results found for IL_BWO9 and IL_BWO10 suggested that those two products had an amorphous structure as a result of too short reaction time.

To further investigate the structure differences in the IL_BWO photocatalysts, Raman spectroscopy was employed (Fig. 3b and S2). The well-defined peaks in the wavenumber in the range of 100–1200 cm^{-1} confirmed the successful formation of the BWO structure. In details, the Raman bands at 720, 796, and 826 cm^{-1} could be assigned to the antisymmetric and symmetric modes of W-O bands. The bands in the range of 110–420 cm^{-1} could be ascribed to the bending modes of WO_6 octahedral with the translational modes of simultaneous Bi^{3+} motions. These results were in line with literature data for materials containing tungstates [31–33]. The peak at 1029 cm^{-1} corresponding to the W═O terminal band was found only in the pristine BWO photocatalyst. The possible reason might be caused by partially disrupted and replaced of the oxygen atoms in the WO_6 octahedral layer by chloride ions [34].

Additionally, the selected-area electron diffraction (SAED) measurements were performed to analyse the phase structure of the selected samples (see Fig. 3c). The results revealed rather the polycrystalline structure than single crystal and were in agreement with the XRD analysis.

The BET surface areas and pore volumes of the as-prepared samples were investigated. The results are displayed in Table 1. As shown, the BET specific surface areas of pristine BWO and KCl_BWO were 39.51 and 49.26 $m^2 \cdot g^{-1}$, respectively, while for IL_BWO3 reached 47.60 $m^2 \cdot g^{-1}$. The highest value was detected for IL_BWO11 (57.43 $m^2 \cdot g^{-1}$), but further extending of the reaction duration caused a reduction in this parameter. The decrease of IL amount resulted in a reduce in the BET specific surface areas from 55.57 to 44.86 $m^2 \cdot g^{-1}$ for IL_BWO1 and IL_BWO5. Increase of the reaction temperature up to 160 °C led to a significant decline of the BET specific surface area to 30.26 $m^2 \cdot g^{-1}$. The values of IL_BWO pore size being slightly larger when higher surface areas were found. It is expected that the increase in the BET surface area of the ultrathin nanosheets will facilitate adsorption of higher number of contaminants on photocatalyst surface, better absorption of light, and thus, improve the photocatalytic performance.

The elemental composition of selected BWO, IL_BWO3 and KCl_BWO photocatalysts were examined by XPS. Both the surface contents (Table 2) and chemical character of Bi, W, O, C, N, and Cl atoms were identified from the corresponding Bi4f, W4f, O1s, C1s, N1s, and Cl2p HR spectra, respectively (Fig. 4). The Bi4f spectra of all samples consisted of three states, represented by $Bi4f_{7/2}$ signals at 159.1–159.4, 156.7–157.1 and 157.4–157.8 eV, respectively (Table 3 and Fig. 4). The first, main state, is identified as Bi(+3) and the next two are assigned to Bi(+3-x) and Bi(0) species [35,36]. The W $4f_{7/2}$ signals at 35.4 and 34.0 eV showed the main contribution of W(+6) compounds and a small amount of W(+4) surface species, respectively [37]. Both signals identified well Bi_2WO_6 [35,36]. The O1s spectra can be separated into three peaks at 529.8–530.1, 530.5–530.8 and 531.6–532.0 eV, which can be attributed to Bi—O, W—O and C—O bounds, respectively [35,37]. The Cl2p spectra confirmed the effective interaction of [TBA][Cl] and KCl with Bi_2WO_6 for corresponding IL_BWO3 and KCl_BWO samples (Fig. 4). The presence of IL species in the surface area of IL_BWO3 composite is also confirmed from N1s spectrum. The small signal at about 395 eV is identified, which is not detected for both BWO and KCl_BWO samples. Thus, we assign this signal to interaction of IL with the surface area of BWO. Such an interaction may initiate the formation of oxygen vacancies in the surface layer of BWO. XPS data seem to support this suggestion. The Bi4f spectrum of the IL_TBA sample shifts by 0.3 eV to higher BE compared to the BWO sample (Fig. 4). Furthermore, the relatively high Bi/O ratio value for the IL_BWO3 sample (Table 2) can be attributed to the partial loss of oxygen atoms due to the interaction with IL.

Zeta potential measurements were performed to investigate the interfacial interaction between chloride ions and BWO surface, and determine their role in the adsorption of aqueous contaminants (Table S2). Compared with pristine BWO, which shown a positively charged surface with zeta potential of approx. 31.8 mV, the zeta potential of the IL_BWO photocatalysts depended on the amount of Cl^- absorbed on the BWO surface, and changed from 25.1 to −14.2 mV for IL_BWO5 and IL_BWO1, respectively. The zeta potential of the photocatalyst prepared in the presence of inorganic salt, KCl_BWO was found to also be negatively charged (-11.2 mV). It can be inferred that those negative charges were found as a consequence of the interaction of BWO with chloride ions, originated from KCl or [TBA][Cl], and strongly depended on the Cl^- ions concentration. As revealed, higher chloride content in KCl_BWO than IL_BWO3 (2.48 and 1.46 at. %, respectively) resulted in more negatively charges surface.

To investigate the photoabsorption properties of the IL_BWO samples, the UV–Vis absorption spectra were taken, and the results are displayed in Fig. 5a and S3. The absorption edge of IL_BWO3 and KCl_BWO were located at similar wavelength at approx. 420 nm for both, while that of the pristine BWO was at marginally higher wavelength of approx. 432 nm. Pristine BWO material exhibited a slight redshift to higher wavelengths compared to all other samples. Analysing the series with different IL content, no apparent changes were observed. Decrease of the reaction temperature slightly deteriorated the optical absorption ability. The absorption properties increased with the reaction duration and final achieve similar effect for the photocatalysts prepared for 12 and 24 h. The corresponding band gap energy (E_g) of pristine and IL_BWO photocatalysts were estimated based on a Tauc plot of $(\alpha h\nu)^{1/2}$ *vs.* photon energy (Table 1). The band gaps (E_g) of IL_BWO samples were in the range of 3.08–3.25 eV depending on the synthesis conditions and being a little wider photocatalysts than pristine BWO (2.93 eV). It can be inferred that the E_g increase was due to the quantum size effect [38,39].

The photoluminescence (PL) spectroscopy was employment to determine the charge separation abilities which could further determine the photocatalytic activity. The results are shown in Fig. 5b and S4. All IL_BWO photocatalyst exhibited similar peak's features with the strongest emission peak at approx. 420 nm which could correspond to the intrinsic Bi^{3+} ions movement from the excited to ground state. The peak placed at approx. 443 nm could be ascribed to the charge transfer between the orbitals of Bi6s and O2p to the empty W5d orbital. The peaks at approx. 455, 481 and 526 nm could be a result of surface defects presence caused by the metal atoms and oxygen vacancies. Moreover, all IL_BWO samples exhibited stronger PL peak intensity compared to pristine BWO photocatalysts. Such kind of results could indicate that in those samples the recombination rate of the photogenerated charge carriers was higher than in pristine BWO. On the other hand, stronger PL peak intensity could be related with higher concentration of the surface oxygen vacancies, suggested by the XPS results. Similar observations were described previously in the literature. For example, Tongay *et al.*, who investigated the effect of defects on the photoluminescence properties of 2D MoS_2, $MoSe_2$, WSe_2 [40], realised that the PL intensity was

Table 2
Elemental composition (in at. %) in the surface layer of pristine BWO, IL_BWO3, and KCl_BWO, evaluated by XPS analysis.

Sample code	Elemental composition (at. %)							Bi/O	Bi/W
	Bi	W	O	C	Cl	N	K		
BWO	26.64	13.10	50.68	9.58	0	0	0	0.52	2.03
IL_BWO3	28.31	13.49	48.23	8.37	1.46	0.14	0	0.59	2.10
KCl_BWO	27.89	13.52	49.99	6.02	2.48	0	0.11	0.56	2.06

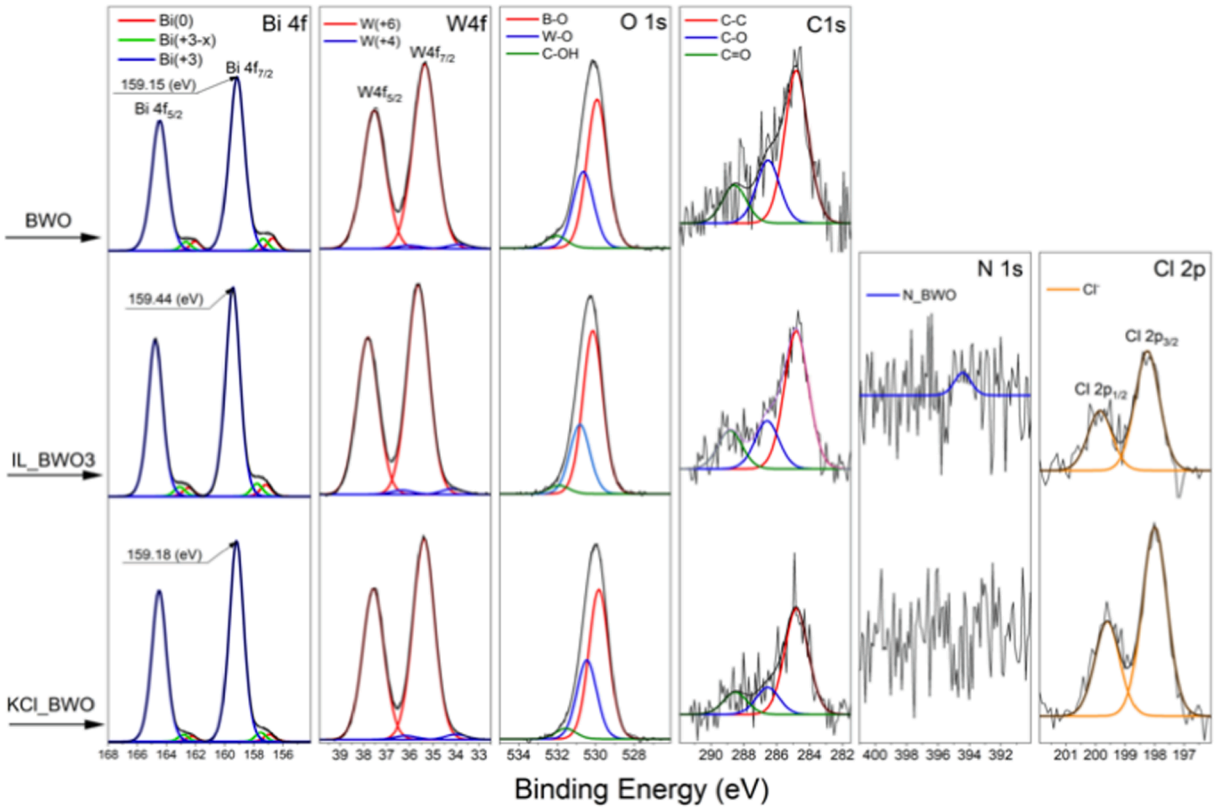

Fig. 4. High resolution Bi4f, W 4f, O1s, C1s, N1s and Cl2p XPS spectra recorded on pristine BWO, IL_BWO3, and KCl_BWO. Parameters used to fit all HR spectra are collected in Table S1.

Table 3
Elemental content and chemical characters of Bi atoms in the surface layers of BWO, IL_BWO3, and KCl_BWO, evaluated by XPS analysis.

Sample code	Bi content (at. %)	Fraction Bi $4f_{7/2}$ state (%)		
		Bi (0)	Bi(+3 − x)	Bi(+3)
		156.7–157.1 eV	157.4 – 157.8 eV	159.1–159.4 eV
BWO	26.64	4.48	4.23	91.29
IL_BWO3	28.31	4.02	4.44	91.54
KCl_BWO	27.84	2.52	3.26	94.22

strengthened due to the presence of defects in compare with pristine materials. Liqiang *et al.* found the inherent relationship between the higher surface oxygen vacancies, the higher PL intensity and the higher photoactivity of ZnO nanoparticles [41]. The surface oxygen vacancies are considered to act as a trapping centre for electrons, which enhances the separation and transport of photogenerated charge carriers [42,43].

3.2. Photocatalytic performance

The photocatalytic activity of the IL_BWO samples was evaluated in the reaction of phenol degradation used as a model aqueous pollutant. The results are shown in Fig. 6a, S5, and Table 1. The blank experiment performed in the photocatalyst absence indicated that the photolysis can be ignored. After 60 min of UV–Vis irradiation the highest photoactivity was found for the ultrathin IL_BWO3 photocatalyst, almost 4 and 2 times higher than KCl_BWO and BWO photocatalysts, respectively. When IL amount decreased, phenol degradation initially grew up, starting from 41 to 86% for IL_BWO1 and IL_BWO3, respectively, and then dropped significantly to 26% for IL_BWO5 (Fig. S5a). The analysis of samples prepared with various reaction temperatures (in the range of 100–160 °C) revealed that the photoactivity was the highest when the photocatalyst was synthesized at 120 °C (86%). At higher temperature the process efficiency started to decrease as a result of crystallinity changes, and finally reached only 14% for IL_BWO8 (almost 6 times worse than of IL_BWO3) (Fig. S5b). The elongation of reaction duration resulted in an increase of the process efficiency almost 5 times (from 18 to 86%) for the IL_BWO9 and IL_BWO3, respectively (Fig. S5c).

The action spectra were measured over IL_BWO3, KCl_BWO and pristine BWO to investigate the exact range of the photoactivity under monochromatic irradiation (Fig. 6b). All samples were active in the range of 380–460 nm, but with different apparent quantum efficiency (AQE). The AQE of IL_BWO3 was 2 times higher than that of KCl_BWO and pristine BWO at the wavelength of 380 nm (21.6, 10.6 and 10.5%, respectively). The photoactivity above wavelength of 440 nm was higher for non-modified sample (AQE 0.75, 0.45, and 0.47% for BWO, KCl_BWO, and IL_BWO3, respectively). The results of AQE and absorption spectra were not located in the same place. However, they show similar trend. As a product of photoabsorption efficiency and electron-positive hole utilization, the AQE depends on those parameters. In an ideal system, the initial rate of photoreaction is proportional to the rate of absorption of the exciting light [44]. However, if the efficiency of photoabsorption is lower, the efficiency of electron hole utilization is higher, the AQE could be shifted to the higher wavelengths.

Additionally, to gain insight into the phenol decomposition pathway, the intermediate products were investigated. The pathway and rate of by-products formation was strongly related with the kinetics of running reaction. The concentration of hydroquinone, benzoquinone and catechol formed over IL_BWO3 was much higher compared to pristine BWO and KCl_BWO (Table S3). The highest initial and constant reaction rate were found for IL_BWO3 (1.90 $\mu mol \bullet mol^{-1} \bullet dm^{-3}$ and 0.0282 min^{-1}) compared to pristine BWO (1.09 $\mu mol \bullet mol^{-1} \bullet dm^{-3}$ and 0.0082 min^{-1}), and KCl_BWO (0.60 $\mu mol \bullet mol^{-1} \bullet dm^{-3}$ and 0.0041 min^{-1}). Those results confirmed that the phenol degradation in the presence of IL_BWO3

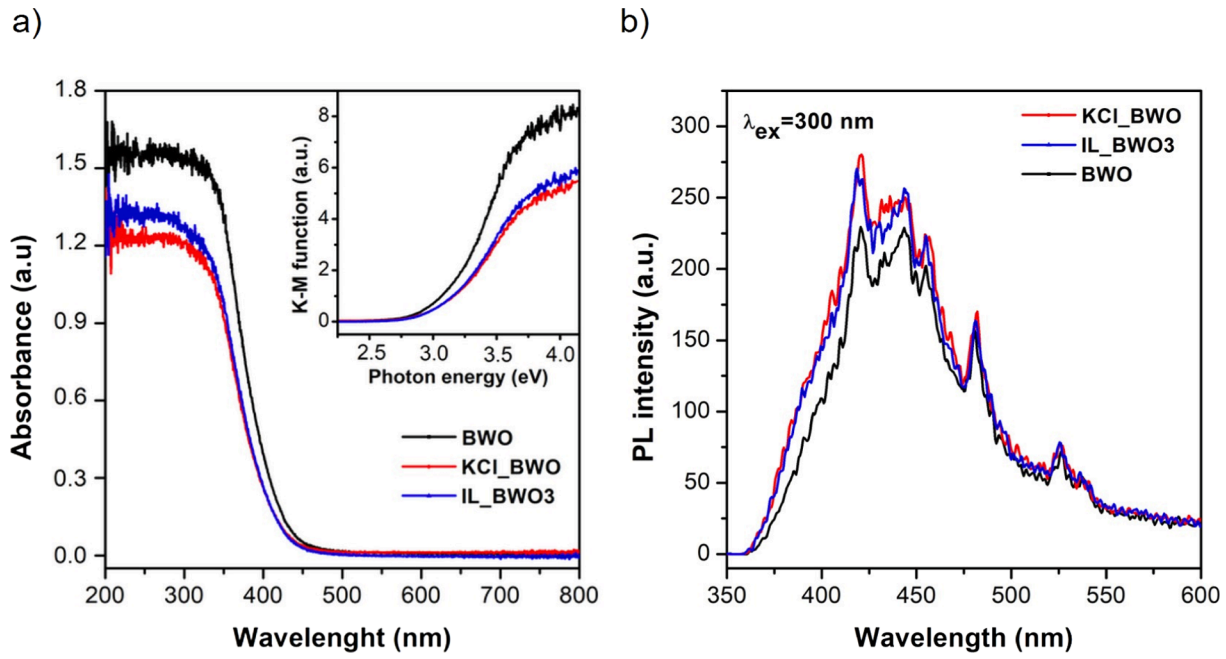

Fig. 5. (a) The optical absorption and (b) PL spectra of the selected BWO photocatalysts.

run faster.

The trapping experiments in the presence of the most photoactive sample, IL_BWO3, were carried out to investigate the active species involved in the photocatalytic phenol degradation. The scavengers, namely *tert*-butanol for •OH, ammonium oxalate for h^+, benzoquinone for $O_2^{\bullet-}$ and silver nitrate for e^-, were added to the phenol solution to confirm their role. As shown in Fig. 6c, the addition of benzoquinone slightly decreased the photodegradation process. Silver nitrate was found to be partially involved in the reaction. The presence of *tert*-butanol and ammonium oxalate significantly inhibited the efficiency of the phenol degradation after 60 min of UV–Vis irradiation implying the dominant role •OH and h^+ in the photocatalytic oxidation reaction.

To provide the information about the long-term practical applications, the stability and reusability tests were performed in four subsequent cycles in the presence of IL_BWO3 under UV–Vis irradiation (Fig. 6d). The process efficiency slightly decreased to 79% after four cycles with only 7% loss when compared to the 1st cycle implying good reusability of those photocatalyst. The XRD analysis of recycled IL_BWO3 revealed high structural stability (Fig. S6). Those slight decline in the XRD peaks intensity could be attributed to the adsorbed organic pollutants on the photocatalyst surface, and thus, reduce the crystallinity.

3.3. Antibacterial properties

The antibacterial activities of selected photocatalysts were evaluated against two types of bacteria, Gram-negative (*E. coli*) and Gram-positive (*S. aureus*) after 180 min of UVA irradiation. The results are displayed in Fig. 7 on the basis of the decrease in the colony number of *E. coli* and *S. aureus* formed on the nutrient agar plate. The control experiments carried out under dark in the presence and absence of photocatalyst showed no reduction of *E. coli* colonies, thereby confirming that the prepared samples were no toxic to *E. coli* and for its inactivation the photocatalytic reaction was required, and no photolysis of bacterial cells under UVA irradiation alone (Fig. 7a). The reduction of *S. aureus* colonies in the absence of photocatalyst under UVA irradiation was observed (Fig. 7b). The dark conditions in the presence and absence of photocatalyst revealed no changes.

As shown, for both bacteria strain the antimicrobial properties were improved when IL was used for the sample preparation. According to the Fig. 7a, the highest *E. coli* inactivation was found for IL_BWO3. Neither pristine BWO and KCl_BWO exhibited any antibacterial activity. Further increase of the IL amount used during the synthesis resulted in reduced *E. coli* inactivation (IL_BWO1) compared with IL_BWO3. Subsequently, the antibacterial activity of the photocatalysts was examined toward the survival of *S. aureus* under UVA light (Fig. 7b). A similar tendency as in the case of *E. coli* inactivation was found and the highest inactivation of *S. aureus* exhibited IL_BWO3 sample. The presence of the IL_BWO3 photocatalyst was not necessary for bacterial inactivation process since *S. aureus* was disinfected under UVA light itself, but its attendance accelerated the process. The enhanced antimicrobial properties of the IL_BWO3 sample was mainly attributed to the following reasons. Given that 2D semiconductors have attracted great attention for the antibacterial applications owing to their layered nanosheet structure, one is the formation of ultrathin criss-crossed nanosheets [45–47]. According to the literature, the crystalline structure of the Bi_2WO_6 nanosheets with a sandwich substructure consisted of $[BiO]^+$-$[WO_4]^{2-}$-$[BiO]^+$ has the ability to promote the separation of the photogenerated electron - hole pairs. Subsequently, those carriers are able to interact in an aqueous environment causing formation of active species (*e.g.,* •OH, $O_2^{\bullet-}$, H^+), which can affect on the bacteria cell's surface and result in damage of its cell membrane [13,45]. Secondly, incorporation of the nitrogen into IL_BWO3 lattice was responsible for the improved antibacterial properties, as it was previously described for the other photocatalysts [48,49]. The presence of IL residues on the photocatalysts surface in combination with the ultrathin IL_BWO3 structure could be responsible for the improved antibacterial activity of the photocatalysts due to the antimicrobial properties of IL [50]. Given the IL_BWO3 sample presented some antimicrobial properties under UVA irradiation on both bacteria strains, Gram-negative and Gram-positive, it suggests a wide range of clinical and environmental applications of IL-based nanomaterials. Such kind of a feature is of great important because of increasing antibacterial mechanism resistance (*e.g.,* change in cell membrane permeability) [51]. The results were consistent with phenol photooxidation process and indicated simultaneous possibility of the application in processes of bacterial deactivation and degradation of organic pollutants.

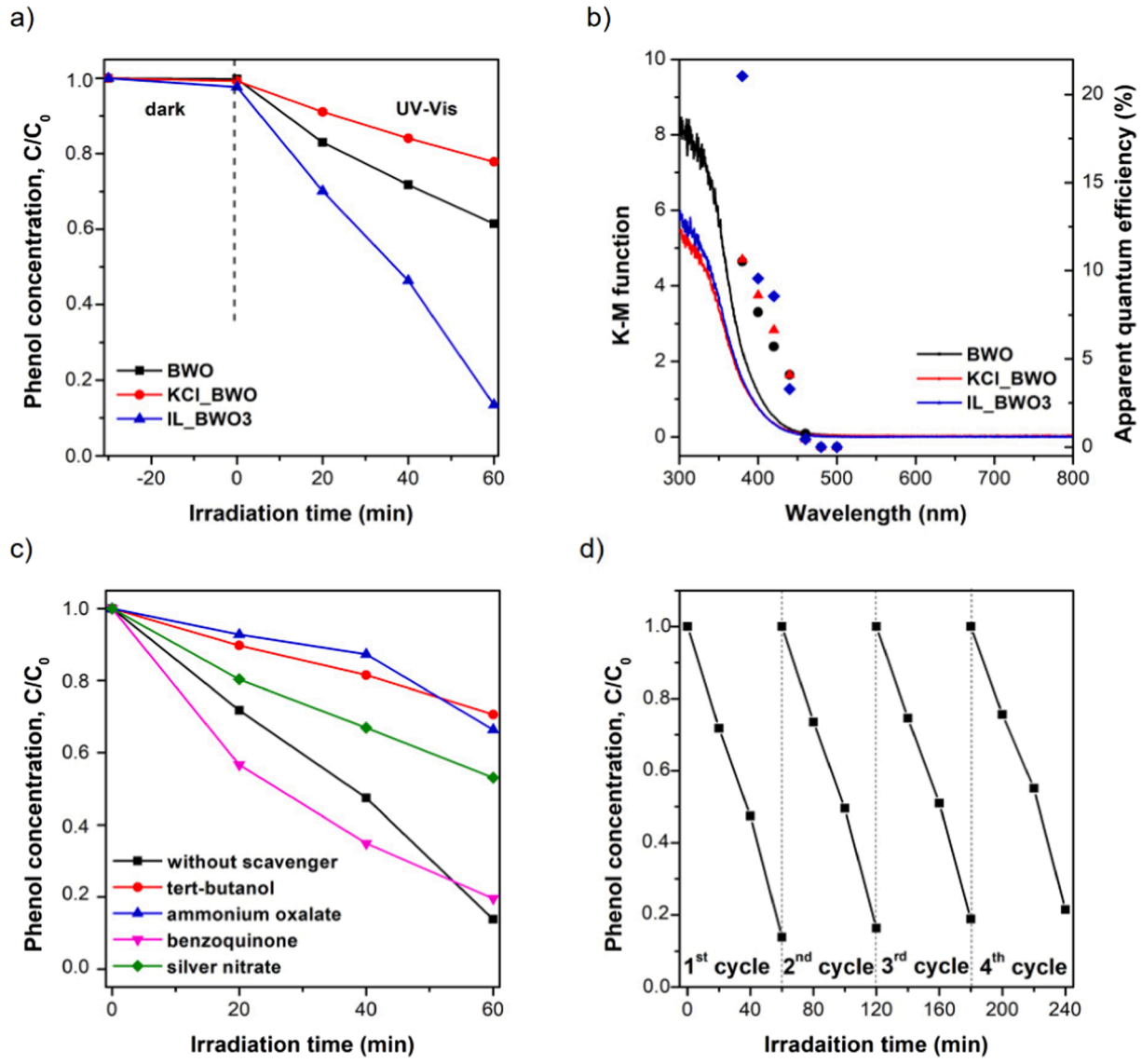

Fig. 6. (a) Phenol degradation efficiency, (b) AS for phenol oxidation (AQE – squares) *vs.* absorption spectrum (K-M function – lines), (c) the trapping experiments with and without scavengers over the most photoactive sample, and (d) photostability of the most photoactive sample in four consecutive cycles.

3.4. Mechanism discussion

To understand the photocatalytic reaction mechanism, it is necessary to consider the factors which could be responsible for the enhancement photocatalytic activity. Starting from the morphology, a significant decrease in the nanosheet thickness in the IL reaction environment was found. The ultrathin nanosheets were found for IL_BWO3 (8 nm), while pristine BWO formed clew-like microspheres. Worth to mentioned that the application of KCl also resulted in the formation of similar dish-like structure with criss-crossed nanosheets with the thickness of 13 nm. Nonetheless, the application of IL could contribute to the presence of surface repulsion forces and steric hindrance from the [TBA] cation, and thus prevented the layers from stacking when comparing to the application of KCl (see Fig. 2). The ultrathin nanosheets formed by IL_BWO3 provided shorter diffusion distance for photoinduced carriers and was beneficial for faster separation and transfer of photogenerated carriers, and thus significantly increased its photocatalytic properties. Similar observations were found by Jiang *et al.* who investigated the influence of 1-hexadecyl-3-methy-limidazolium bromine on the formation and photocatalytic performance of the ultrathin BiOBr nanosheets [23]. Besides, almost unchanged crystallinity, optical properties and surface areas of the IL_BWO3 and KCl_BWO samples suggests that they were not the main factors responsible for the enhancement photocatalytic performance.

In addition, it was important to investigate the effect of surface charge generated on the photocatalysts surface in order to understand the possible phenol degradation mechanism. As revealed, the Zeta potential of the IL_BWO3 photocatalysts was negatively charged (-7.6 eV), in opposite to pristine BWO (+31.8 eV). According to the literature data, the negatively charged photocatalysts should be able to adsorb positively charged molecules [13,52]. Phenol, as an acidic species, undergoes dissociation leading to the appearance of the hydrogen ion (H^+) and phenoxide ion ($C_6H_5O^-$). Therefore, adsorption of phenol on the photocatalyst surface might get supressed because of the appearance of electronic repulsion between the phenol and photocatalyst surface resulting from negative charge on the surface of both of them. Interestingly, phenol degradation efficiency of IL_BWO3 was significantly improved (almost 2 and 4 times than that of pristine BWO and KCl_BWO, respectively). Given by the XPS results, the effective interaction of both chloride source (owing to the strong Cl2p spectra) suggests that Cl^- ions were bonded to the surface of both, IL_BWO3 and KCl_BW, was confirmed. However, in the case of IL_BWO3 the presence of N1s spectra

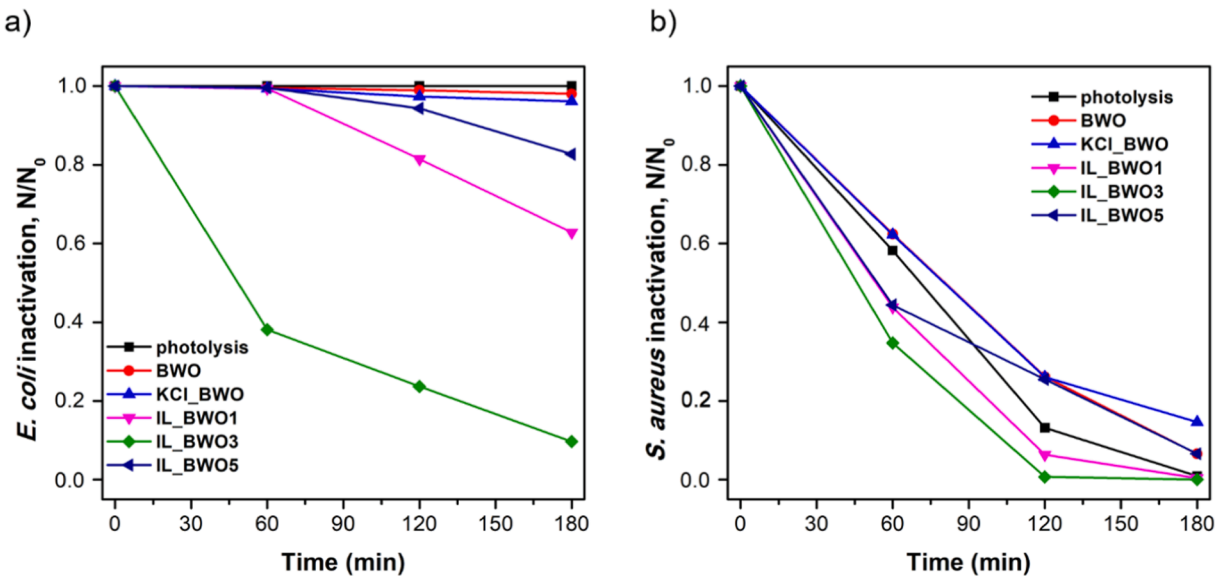

Fig. 7. Photocatalytic inactivation of (a) *E. coli* and (b) *S. aureus* in aqueous dispersions of the selected IL_BWO samples under UVA irradiation. Experimental conditions: photocatalyst concentration: 250 mg/L, initial bacteria concentration: 10^3 CFU/mL, and irradiation intensity: 11.5 mW/cm^2.

proved successful interaction of IL residues with BWO surface (Table 2). Such kind of feature could initiate formation of oxygen vacancies, in agreement with the PL results where the increase in the PL intensity could result from a higher oxygen vacancies concentration [53] (see Fig. 5b). Thereby, the improved photocatalytic performance of IL_BWO3 was related to higher concentration of oxygen vacancies and their ability to facilitate the photooxidation reaction [54].

To look deeper, the band edge potentials of IL_BWO3 were estimated based on the equations of the conduction band potential (E_{CB}) and the valence band potential (E_{VB}), $E_{CB} = X - E_c - \frac{1}{2}E_g$ an $E_{VB} = E_{CB} + E_g$, respectively. The X is the electronegativity of the Bi_2WO_6 photocatalyst (*ca.* 6.36 eV). E_C is the energy of free electrons on the scale (4.5 eV). The E_g of IL_BWO3 was determined based on the DRS spectra and was approx. 3.03 eV, slightly higher than that of pristine BWO (2.93 eV) which could be related with the quantum-size effect (Fig. 5). The VB and CB were estimated approx. 3.38 eV and 0.41 eV. As shown in Fig. 8, the CB potential of IL_BWO3 was more positive than $E^0(O_2/O_2^{\bullet-})$, thus the photogenerated electrons could not reduce O_2 to generate $O_2^{\bullet-}$ and the VB potential was much higher than $E^0(\bullet OH/H_2O)$ so that, under UV–Vis irradiation, the photogenerated holes were able to oxidize H_2O to produce •OH. A similar process of the reaction mechanism has already been described in the literature [55–57]. This was in agreement with the result of the trapping experiments, where •OH and h^+ were the main species responsible for the photooxidation process whereas, the photogenerated electrons whose role was much less prominent, for the reduction reactions. It can be assumed that the photogenerated electrons might more recombined with holes, since they were not energetic enough to react with oxygen molecules. On the other hand, the ability of holes to generate •OH suggests that only some of them were involved in the recombination process, while the others were used in the photocatalytic oxidation. A possible process of the photogenerated electrons consumption could proceed in a two electron-reduction, as follows:

$$e^- + O_2 + H^+ \rightarrow HO_2^{\bullet} \quad (1)$$

$$e^- + HO_2^{\bullet} + H^+ \rightarrow H_2O_2 \quad (2)$$

$$2e^- + O_2 + 2H^+ \rightarrow H_2O_2 \quad (3)$$

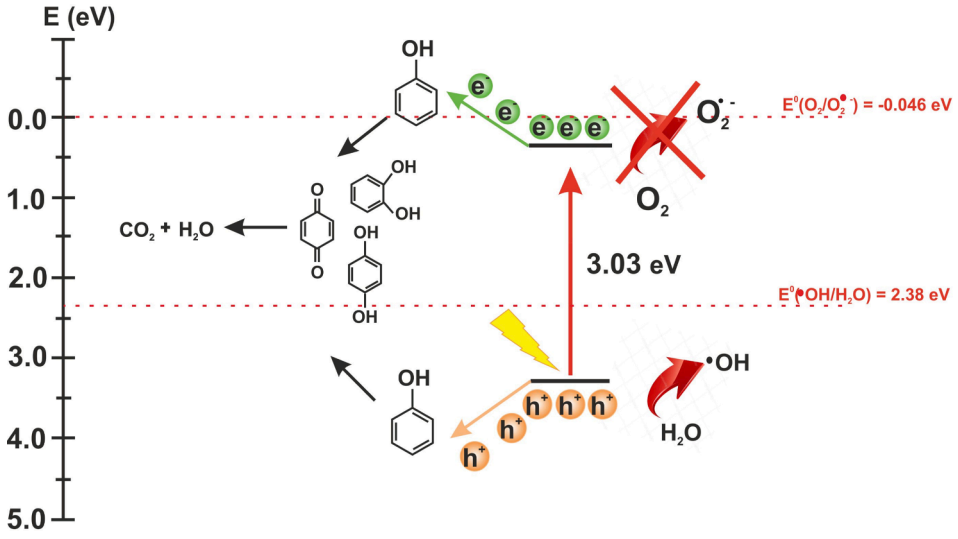

Fig. 8. Photocatalytic mechanism scheme of IL_BWO3 under UV–Vis irradiation.

$$e^- + H_2O_2 + H^+ \rightarrow \bullet OH + H_2O \quad (4)$$

It can be assumed that the same mechanism as of for phenol degradation could be responsible for the enhanced antimicrobial properties of IL_BWO3 sample, since the presence of hydroxyl radicals and holes has been related to the damage of cell membranes, thus supressing the growth of bacteria [58–60].

4. Conclusions

In summary, the ultrathin IL_BWO photocatalysts were successfully synthesised *via* ionic liquid-assisted hydrothermal method by adjusting the amount of [TBA][Cl], synthesis temperature and duration. The application of IL facilitated formation of the ultrathin nanosheets with the thickness of 8 nm, while its absence caused the growth of clew-like microspheres with average diameter of 3.39 μm. Moreover, by selecting the amount of IL, the control of the nanosheet thickness was possible due to the morphology-directing role of IL. The replacement of IL with KCl led to the formation of similar structure of criss-crossed nanosheets with the thickness of 13 nm. Comparing the crystallinity, optical properties and surface areas of the ultrathin IL_BWO3 and KCl_BWO, almost unchanged results were found. The presence of nitrogen form IL decomposition contributed to the initial formation of oxygen vacancies as was confirmed by XPS and PL analysis. The ultrathin nanosheets exhibited improved photocatalytic performance for phenol degradation compared to pristine BWO and KCl_BWO (almost 2 and 4 times, respectively), demonstrating the key role of IL in the enhanced photocatalytic properties. Thereby, the results indicated that both, cation and anion, have synergic effect on the growth and properties of the nanosheet structure. The trapping experiments revealed the major role •OH and h^+ involved in the photocatalytic reaction in the presence of ultrathin IL_BWO nanosheets under UV–Vis irradiation. The presence of hydroxyl radicals could be also responsible for the enhanced antimicrobial properties toward two kind of bacteria strain, *E. coli* and *S. aureus*. The improved photocatalytic properties were attributed to (i) the ultrathin structure, which let for shorter diffusion distance, (ii) the nitrogen presence on the photocatalyst surface, and finally, (iii) the oxygen vacancies formation. Furter efforts are needed to prepare ultrathin IL_BWO nanosheets and improve their photocatalytic performance.

CRediT authorship contribution statement

Anna Pancielejko: Conceptualization, Methodology, Investigation, Writing – original draft, Project administration, Funding acquisition. **Justyna Łuczak:** Conceptualization, Methodology, Writing – review & editing, Supervision. **Wojciech Lisowski:** Investigation, Writing – original draft. **Grzegorz Trykowski:** Investigation, Writing – original draft. **Danae Venieri:** Investigation, Writing – original draft. **Adriana Zaleska-Medynska:** Supervision. **Paweł Mazierski:** Conceptualization, Methodology, Writing – original draft, Supervision.

Declaration of Competing Interest

The authors declare that they have no known competing financial interests or personal relationships that could have appeared to influence the work reported in this paper.

Acknowledgements

This work was supported by realises a project co-financed from European Funds 'Integrated Programme of Development of Gdańsk University of Technology', POWR.03.05.00-00-Z044/17. A. P. gratefully acknowledge financial support for the research fellowship at Technical University of Crete, School of Environmental Microbiology, financed by Gdansk University of Technology by InterPhD II (PO WER) project (No. POWR.03.02.00-IP.08-00-DOK/16).

Appendix A. Supplementary material

Supplementary data to this article can be found online at https://doi.org/10.1016/j.apsusc.2022.153971.

References

[1] P. Ganguly, M. Harb, Z. Cao, L. Cavallo, A. Breen, S. Dervin, D.D. Dionysiou, S. C. Pillai, 2D Nanomaterials for Photocatalytic Hydrogen Production, ACS Energy Lett. 4 (2019) 1687–1709, https://doi.org/10.1021/acsenergylett.9b00940.
[2] Y. Chen, G. Jia, Y. Hu, G. Fan, Y.H. Tsang, Z. Li, Z. Zou, Two-dimensional nanomaterials for photocatalytic CO2 reduction to solar fuels, Sustain. Energy Fuels 1 (2017) 1875–1898, https://doi.org/10.1039/c7se00344g.
[3] W. Wang, J.C. Yu, D. Xia, P.K. Wong, Y. Li, Graphene and g-C3N4 Nanosheets Cowrapped Elemental α-Sulfur As a Novel Metal-Free Heterojunction Photocatalyst for Bacterial Inactivation under Visible-Light, Environ. Sci. Technol. 47 (2013) 8724–8732, https://doi.org/10.1021/es4013504.
[4] H. Li, J. Shang, Z. Ai, L. Zhang, Efficient visible light nitrogen fixation with BiOBr nanosheets of oxygen vacancies on the exposed 001 Facets, J. Am. Chem. Soc. 137 (2015) 6393–6399, https://doi.org/10.1021/jacs.5b03105.
[5] H. Lv, Y. Huang, R.T. Koodali, G. Liu, Y. Zeng, Q. Meng, M. Yuan, Synthesis of Sulfur-Doped 2D Graphitic Carbon Nitride Nanosheets for Efficient Photocatalytic Degradation of Phenol and Hydrogen Evolution, ACS Appl. Mater. Interfaces 12 (2020) 12656–12667, https://doi.org/10.1021/acsami.9b19057.
[6] W. Zhao, J. Liu, Z. Ding, J. Zhang, X. Wang, Optimal synthesis of platinum-free 1D/2D CdS/MoS2 (CM) heterojunctions with improved photocatalytic hydrogen production performance, J. Alloys Compd. 813 (2020), 152234, https://doi.org/10.1016/j.jallcom.2019.152234.
[7] C. Tan, X. Cao, X.J. Wu, Q. He, J. Yang, X. Zhang, J. Chen, W. Zhao, S. Han, G. H. Nam, et al., Recent Advances in Ultrathin Two-Dimensional Nanomaterials, Chem. Rev. 117 (2017) 6225–6331, https://doi.org/10.1021/acs.chemrev.6b00558.
[8] R. Mas-Ballesté, C. Gómez-Navarro, J. Gómez-Herrero, F. Zamora, 2D materials: To graphene and beyond, Nanoscale 3 (2011) 20–30, https://doi.org/10.1039/c0nr00323a.
[9] L. Sheng, T. Liao, L. Kou, Z. Sun, Single-crystalline ultrathin 2D TiO2 nanosheets: A bridge towards superior photovoltaic devices, Mater. Today Energy 3 (2017) 32–39, https://doi.org/10.1016/j.mtener.2016.12.004.
[10] Y. Zhao, N. Liu, S. Zhou, J. Zhao, Two-dimensional ZnO for the selective photoreduction of CO2, J. Mater. Chem. A 7 (2019) 16294–16303, https://doi.org/10.1039/c9ta04477a.
[11] K. Xu, L. Wang, X. Xu, S.X. Dou, W. Hao, Y. Du, Two dimensional bismuth-based layered materials for energy-related applications, Energy Storage Mater. 19 (2019) 446–463, https://doi.org/10.1016/j.ensm.2019.03.021.
[12] M.D. Prasad, G.V. Ramesh, S.K. Batabyal, 2D Layered Structure of Bismuth Oxyhalides for Advanced Applications, ACS Symp. Ser. 1353 (2020) 295–315, https://doi.org/10.1021/bk-2020-1353.ch012.
[13] Y. Zhou, Y. Zhang, M. Lin, J. Long, Z. Zhang, H. Lin, J.C.S. Wu, X. Wang, Monolayered Bi2WO6 nanosheets mimicking heterojunction interface with open surfaces for photocatalysis, Nat. Commun. 6 (2015) 1–8, https://doi.org/10.1038/ncomms9340.
[14] D. Sun, Y. Le, C. Jiang, B. Cheng, Ultrathin Bi2WO6 nanosheet decorated with Pt nanoparticles for efficient formaldehyde removal at room temperature, Appl. Surf. Sci. 441 (2018) 429–437, https://doi.org/10.1016/j.apsusc.2018.02.001.
[15] Y. Liang, J. Shi, Effect of Halide Ions on the Microstructure of Bi2WO6 with Enhanced Removal of Rhodamine B, J. Inorg. Organomet. Polym Mater. 30 (2020) 2872–2880, https://doi.org/10.1007/s10904-019-01437-0.
[16] Y. Jiang, H.Y. Chen, J.Y. Li, J.F. Liao, H.H. Zhang, X.D. Wang, D. Kuang, Bin Z-Scheme 2D/2D Heterojunction of CsPbBr 3/Bi2WO6 for Improved Photocatalytic CO2 Reduction, Adv. Funct. Mater. 30 (2020) 2–9, https://doi.org/10.1002/adfm.202004293.
[17] K. Mallikarjuna, H. Kim, Bandgap-tuned ultra-small SnO2-nanoparticle-decorated 2D-Bi2WO6 nanoplates for visible-light-driven photocatalytic applications, Chemosphere 263 (2021), 128185, https://doi.org/10.1016/j.chemosphere.2020.128185.
[18] A.P. Jakhade, M.V. Biware, R.C. Chikate, Two-dimensional Bi2WO6 nanosheets as a robust catalyst toward photocyclization, ACS Omega 2 (2017) 7219–7229, https://doi.org/10.1021/acsomega.7b01086.
[19] J. Łuczak, M. Paszkiewicz, A. Krukowska, A. Malankowska, A. Zaleska-Medynska, Ionic liquids for nano- and microstructures preparation. Part 1: Properties and multifunctional role, Adv. Colloid Interface Sci. 230 (2016) 13–28, https://doi.org/10.1016/j.cis.2015.08.006.
[20] J. Łuczak, M. Paszkiewicz, A. Krukowska, A. Malankowska, A. Zaleska-Medynska, Ionic liquids for nano- and microstructures preparation. Part 2: Application in synthesis, Adv. Colloid Interface Sci. 227 (2016) 1–52, https://doi.org/10.1016/J.CIS.2015.08.010.
[21] L. Dou, Y. Xiang, J. Zhong, J. Li, S. Huang, Ionic liquid-assisted preparation of thin Bi2SiO5 nanosheets for effective photocatalytic degradation of RhB, Mater. Lett. 261 (2020), 127117, https://doi.org/10.1016/j.matlet.2019.127117.
[22] J. Xia, M. Ji, J. Di, B. Wang, S. Yin, M. He, Q. Zhang, H. Li, Improved photocatalytic activity of few-layer Bi4O5I2 nanosheets induced by efficient charge separation and lower valence position, J. Alloys Compd. 695 (2017) 922–930, https://doi.org/10.1016/j.jallcom.2016.10.203.

[23] Q. Jiang, M. Ji, R. Chen, Y. Zhang, K. Li, C. Meng, Z. Chen, H. Li, J. Xia, Ionic liquid induced mechanochemical synthesis of BiOBr ultrathin nanosheets at ambient temperature with superior visible-light-driven photocatalysis, J. Colloid Interface Sci. 574 (2020) 131–139, https://doi.org/10.1016/j.jcis.2020.04.018.
[24] Q. Zhu, Z. Wang, L. Chen, H. Cheng, Z. Qi, Ionic-Liquid-Controlled Two-Dimensional Monolayer Bi2MoO6 and Its Adsorption of Azo Molecules, ACS Appl. Nano Mater. 1 (2018) 5083–5091, https://doi.org/10.1021/acsanm.8b01186.
[25] M.K. Jana, K. Biswas, C.N.R. Rao, Ionothermal synthesis of few-layer nanostructures of Bi2Se3 and related materials, Chem. - A Eur. J. 19 (2013) 9110–9113, https://doi.org/10.1002/chem.201300983.
[26] S. Yin, Y. Ding, C. Luo, Q. Hu, Y. Chen, J. Di, B. Wang, J. Xia, H. Li, Construction of 2D/2D MoS2/PbBiO2Cl nanosheet photocatalysts with accelerated interfacial charge transfer for boosting visible light photocatalytic activity, Colloids Surfaces A Physicochem. Eng. Asp. 609 (2021), 125655, https://doi.org/10.1016/j.colsurfa.2020.125655.
[27] J. Zhao, M. Ji, J. Di, Y. Ge, P. Zhang, J. Xia, H. Li, Synthesis of g-C3N4/Bi4O5Br 2 via reactable ionic liquid and its cooperation effect for the enhanced photocatalytic behavior towards ciprofloxacin degradation, J. Photochem. Photobiol. A Chem. 347 (2017) 168–176, https://doi.org/10.1016/j.jphotochem.2017.07.023.
[28] Prevac Sample holder. https://www.prevac.eu/en/2,offer/36,sample-holders,3.html (access February 10, 2022).
[29] K. Jing, J. Xiong, N. Qin, Y. Song, L. Li, Y. Yu, S. Liang, L. Wu, Development and photocatalytic mechanism of monolayer Bi2MoO6 nanosheets for the selective oxidation of benzylic alcohols, Chem. Commun. 53 (2017) 8604–8607, https://doi.org/10.1039/c7cc04052k.
[30] F. Xu, H. Chen, C. Xu, D. Wu, Z. Gao, Q. Zhang, K. Jiang, Ultra-thin Bi2WO6 porous nanosheets with high lattice coherence for enhanced performance for photocatalytic reduction of Cr(VI), J. Colloid Interface Sci. 525 (2018) 97–106, https://doi.org/10.1016/j.jcis.2018.04.057.
[31] Phuruangrat, A.; Dumrongrojthanath, P.; Ekthammathat, N.; Thongtem, S.; Thongtem, T. Hydrothermal Synthesis, Characterization, and Visible Light-Driven Photocatalytic Properties of Bi2WO6 Nanoplates, vol. 2014, 2014. https://10.1155/2014/138561.
[32] C. Santato, M. Odziemkowski, M. Ulmann, J. Augustynski, Crystallographically oriented mesoporous WO3 films: Synthesis, characterization, and applications, J. Am. Chem. Soc. 123 (2001) 10639–10649, https://doi.org/10.1021/ja011315x.
[33] R. Adhikari, H.M. Trital, A. Rajbhandari, J. Won, S.W. Lee, Microwave induced morphology evolution of bismuth tungstate photocatalyst: Evaulation of phocatalytic activity under visible light, J. Nanosci. Nanotechnol. 15 (2015) 7249–7253, https://doi.org/10.1166/jnn.2015.10576.
[34] X. Cao, Z. Chen, R. Lin, W.C. Cheong, S. Liu, J. Zhang, Q. Peng, C. Chen, T. Han, X. Tong, et al., A photochromic composite with enhanced carrier separation for the photocatalytic activation of benzylic C-H bonds in toluene, Nat. Catal. 1 (2018) 704–710, https://doi.org/10.1038/s41929-018-0128-z.
[35] Y. Lv, W. Yao, R. Zong, Y. Zhu, Fabrication of wide-range-visible photocatalyst Bi2WO6-x nanoplates via surface oxygen vacancies, Sci. York 6 (2016) 1–9, https://doi.org/10.1038/srep19347.
[36] L.H. Hoang, N.D. Phu, H. Peng, X.B. Chen, High photocatalytic activity N-doped Bi2WO6 nanoparticles using a two-step microwave-assisted and hydrothermal synthesis, J. Alloys Compd. 744 (2018) 228–233, https://doi.org/10.1016/j.jallcom.2018.02.094.
[37] Naumkin, A. V.; Kraut-Vass, A.; Gaarenstroom, S.W.; Powell, C.J. NIST X-ray Photoelectron Spectroscopy Database 20 Version 4.1.2012.
[38] K. Manjunath, L.S. Reddy Yadav, T. Jayalakshmi, V. Reddy, H. Rajanaika, G. Nagaraju, Ionic liquid assisted hydrothermal synthesis of TiO2 nanoparticles: photocatalytic and antibacterial activity, J. Mater. Res. Technol. 7 (2018) 7–13, https://doi.org/10.1016/j.jmrt.2017.02.001.
[39] Z. Zhu, S. Wan, Y. Zhao, Y. Qin, X. Ge, Q. Zhong, Y. Bu, Recent progress in Bi2WO6-based photocatalysts for clean energy and environmental remediation: Competitiveness, challenges, and future perspectives, Nano Sel. 2 (2021) 187–215, https://doi.org/10.1002/nano.202000127.
[40] S. Tongay, J. Suh, C. Ataca, W. Fan, A. Luce, J.S. Kang, J. Liu, C. Ko, R. Raghunathanan, J. Zhou, et al., Defects activated photoluminescence in two-dimensional semiconductors: interplay between bound, charged, and free excitons, Sci. Rep. 2 (2013) 2657, https://doi.org/10.1038/srep02657.
[41] J. Liqiang, Y. Fulong, H.O.U. Haige, X.I.N. Baifu, C.A.I. Weimin, Relationships of surface oxygen vacancies with photoluminescence and photocatalytic performance of ZnO nanoparticles, Sci. China, Ser. B Chem. 48 (2005) 25–30, https://doi.org/10.1360/03yb0191.
[42] H. Chen, C. Zhang, Y. Pang, Q. Shen, Y. Yu, Y. Su, J. Wang, F. Zhang, H. Yang, Oxygen vacancy regulation in Nb-doped Bi2WO6 for enhanced visible light photocatalytic activity, RSC Adv. 9 (2019) 22559–22566, https://doi.org/10.1039/c9ra02862e.
[43] Y. Liu, B. Wei, L. Xu, H. Gao, M. Zhang, Generation of Oxygen Vacancy and OH Radicals: A Comparative Study of Bi2WO6 and Bi2WO6-x Nanoplates, ChemCatChem 7 (2015) 4076–4084, https://doi.org/10.1002/cctc.201500714.
[44] B. Ohtani, Photocatalysis A to Z-What we know and what we do not know in a scientific sense, J. Photochem. Photobiol. C Photochem. Rev. 11 (2010) 157–178, https://doi.org/10.1016/j.jphotochemrev.2011.02.001.
[45] M. Karollyna, S. Leandro, B. Moura, P. De Tarso, C. Freire, M.L. Vega, L. Lima, Á. A. Hidalgo, A. Carolina, J. De Ara, et al., Characterization and evaluation of layered Bi2WO6 nanosheets as a new antibacterial agent, Antibiotics 10 (2021) 1068, https://doi.org/10.3390/antibiotics10091068.
[46] J. Chen, H. Peng, X. Wang, F. Shao, Z. Uuan, H. Huan, Graphene oxide exhibits broad-spectrum antimicrobial activity against bacterial phytopathogens and fungal conidia by intertwining and membrane perturbation, Nanoscale 6 (2014) 1879–1889, https://doi.org/10.1039/c3nr04941h.
[47] J. Zeng, Z. Li, H. Jiang, X. Wang, Progress on photocatalytic semiconductor hybrids for bacterial inactivation, Mater. Horizons 8 (2021) 2964–3008, https://doi.org/10.1039/d1mh00773d.
[48] T. Makropoulou, P. Panagiotopoulou, D. Venieri, N-doped TiO2 photocatalysts for bacterial inactivation in water, J. Chem. Technol. Biotechnol. 93 (2018) 2518–2526, https://doi.org/10.1002/jctb.5639.
[49] M. Tio, L. Irradiation, M. Janus, E. Kusiak-nejman, P. Rokicka-konieczna, A. W. Morawski, Bacterial Inactivation on Concrete Plates Loaded with Modified TiO2 Photocatalysts under Visible Light Irradiation, Molecules 24 (2019) 3026.
[50] J.N. Pendleton, B.F. Gilmore, The antimicrobial potential of ionic liquids: A source of chemical diversity for infection and biofilm control, Int. J. Antimicrob. Agents 46 (2015) 131–139, https://doi.org/10.1016/j.ijantimicag.2015.02.016.
[51] Y. Paitan, Current Trends in Antimicrobial Resistance of Escherichia coli, Springer, Cham, 2018.
[52] S. Sharma, N. Khare, Hierarchical Bi2S3 nanoflowers: A novel photocatalyst for enhanced photocatalytic degradation of binary mixture of Rhodamine B and Methylene blue dyes and degradation of mixture of p-nitrophenol and p-chlorophenol, Adv. Powder Technol. 29 (2018) 3336–3347, https://doi.org/10.1016/j.apt.2018.09.012.
[53] L.-Q. Jing, B.-F. Xin, D.-J. Wang, F.-L. Yuan, H.-G. Fu, C.-C. Sun, Relationships between photoluminescence performance and photocatalytic activity of ZnO and TiO2 nanoparticles, Chem. Res. Chin. Univ. 26 (2005) 111–115.
[54] Z. Wei, R. Li, R. Wang, Enhanced visible light photocatalytic activity of BiOBr by: In situ reactable ionic liquid modification for pollutant degradation, RSC Adv. 8 (2018) 7956–7962, https://doi.org/10.1039/c7ra13779f.
[55] Q. Sun, X. Jia, X. Wang, H. Yu, J. Yu, Facile synthesis of porous Bi2WO6 nanosheets with high photocatalytic performance, Dalt. Trans. 44 (2015) 14532–14539, https://doi.org/10.1039/C5DT01859E.
[56] T. Saison, P. Gras, N. Chemin, C. Chanéac, O. Durupthy, V. Brezová, C. Colbeau-Justin, J.P. Jolivet, New insights into Bi2WO6 properties as a visible-light photocatalyst, J. Phys. Chem. C 117 (2013) 22656–22666, https://doi.org/10.1021/jp4048192.
[57] J. Sheng, X. Li, Y. Xu, Generation of H2O2 and OH Radicals on Bi2WO6 for Phenol Degradation under Visible Light, ACS Catal. 4 (2014) 732–737, https://doi.org/10.1021/cs400927w.
[58] M.A. Gondal, A. Bagabas, A. Dastageer, A. Khalil, Synthesis, characterization, and antimicrobial application of nano-palladium-doped nano-WO3, J. Mol. Catal. A: Chem. 323 (2010) 78–83, https://doi.org/10.1016/j.molcata.2010.03.019.
[59] I. Sherman, Y. Gerchman, Y. Sasson, H. Gnayem, H. Mamane, Disinfection and Mechanistic Insights of E. coli in Water by Bismuth Oxyhalide Photocatalysis, Am. Soc. Photobiol. 92 (2016) 826–834, https://doi.org/10.1111/php.12635.
[60] M. Karbasi, F. Karimzadeh, K. Raeissi, S. Rtmi, J. Kiwi, S. Giannakis, C. Pulgarin, Insights into the Photocatalytic Bacterial Inactivation by Flower-Like Bi2WO6 under Solar or Visible Light, Through in Situ Monitoring and Determination of Reactive Oxygen Species (ROS), Water 12 (2020) 1099, https://doi.org/10.3390/w12041099.